

Explosive chromospheric evaporation driven by nonthermal electrons around one footpoint of a solar flare loop

D. Li^{1,2,3}, Z. J. Ning¹, Y. Huang¹, and Q. M. Zhang^{1,2}

¹*Key Laboratory of Dark Matter and Space Astronomy, Purple Mountain Observatory, CAS, Nanjing 210008, China*

²*CAS Key Laboratory of Solar Activity, National Astronomical Observatories, Beijing 100012, China*

³*Key Laboratory of Modern Astronomy and Astrophysics (Nanjing University), Ministry of Education, Nanjing 210023, China*

ABSTRACT

We explore the temporal relationship between microwave/HXR emission and Doppler velocity during the impulsive phase of a solar flare on 2014 October 27 (SOL2014-10-27), which displays a pulse on the light curves in microwave (34 GHz) and hard X-ray (HXR, 25–50 keV) bands before the flare maximum. Imaging observation shows that this pulse mainly comes from one footpoint of a solar flare loop. The slit of *Interface Region Imaging Spectrograph* (IRIS) stays at this footpoint during this solar flare. The Doppler velocities of Fe xxI 1354.09 Å and Si iv 1402.77 Å are extracted from the Gaussian fitting method. We find that the hot line of Fe xxI 1354.09 Å ($\log T \sim 7.05$) in corona exhibits blue shift, while the cool line of Si iv 1402.77 Å ($\log T \sim 4.8$) in transition region exhibits red shift, indicating explosive chromospheric evaporation. The evaporative upflows along the flare loop are also observed in the AIA 131 Å image. To our knowledge, this is the first report of chromospheric evaporation evidence from both spectral and imaging observations in the same flare. Both microwave and HXR pulses are well correlated with the Doppler velocities, suggesting that the chromospheric evaporation is driven by nonthermal electrons around this footpoint of a solar flare loop.

Subject headings: Sun: flares — Sun: UV radiation — Sun: radio radiation — Sun: X-rays, gamma rays — line: profiles

1. Introduction

In a typical solar flare, the released energy is about 10^{30} erg within dozens of minutes. Such huge energy is thought to be transferred from the magnetic energy via reconnection, which is thought to heat the plasma and to accelerate the bi-directional nonthermal electrons through the solar chromosphere, transition region and corona. This is well known as the standard solar flare model. These accelerated electrons are guided by the newly reconnected magnetic field lines. Some of the accelerated electrons travel up to the interplanetary space, and the others propagate downward to the lower corona and upper chromosphere,

where they lose their energies through Coulomb collisions with the denser plasma. Subsequently, two footpoint sources are often produced along the flare loop legs in the hard X-ray (HXR) and microwave bands (Brown 1971; Asai et al. 2006), and the double ribbons are brightened in H α , ultraviolet (UV), and extreme-ultraviolet (EUV) wavelengths (Czaykowska 1999; Del Zanna et al. 2006; Milligan 2015). Meanwhile, the local chromospheric material is rapidly heated up to ~ 10 MK (Antonucci et al. 1982), resulting in a higher pressure, which drives the chromospheric material upward into the corona along the solar flare loops. Thus the hot plasma fills the solar flare loops in a process called ‘chromospheric evaporation’ (Brown 1973; Fisher et al. 1985a,b; Liu et al.

³Correspondence should be sent to: lidong@pmo.ac.cn.

2006; Ning & Cao 2010; Brosius & Daw 2015; Tian et al. 2015; Young et al. 2015; Zhang et al. 2016; Lee et al. 2017). At the same time, the overpressure also drives the denser plasma downward into the lower chromosphere in a process called ‘chromospheric condensation’ (Fisher et al. 1985a,b; Teriaca et al. 2006; Li et al. 2015).

Chromospheric evaporation is observed in multiple wavelengths, i.e., HXR, EUV/UV, and microwave bands. Imaging observations show that the HXR emission tends to rise with the double footpoint sources along the loop legs, eventually merging them into a single source at the loop top (e.g., Liu et al. 2006; Ning & Cao 2010; Ning 2011; Nitta et al. 2012). This process is thought to be the HXR signature of chromospheric evaporation. On the other hand, the heated materials rise upward to the corona and disturb the local plasma. This process causes the microwave emission suddenly cut-off on the dynamic spectra. Observationally, a high-frequency cut-off drifts to low-frequency is the radio signature of chromospheric evaporation (Aschwanden & Benz 1995; Karlicky 1998; Ning et al. 2009). Joint observations from spectra and images show that the blue shift of hot lines in corona tends to appear at the outside of flare ribbon (Czaykowska 1999; Li & Ding 2004; Li et al. 2015).

Chromospheric evaporation is divided into two types, i.e., ‘explosive’ and ‘gentle’. Explosive evaporation takes place if the input energy flux exceeds a critical value of $\sim 10^{10}$ erg cm $^{-2}$ s $^{-1}$ (Fisher et al. 1985a,b). In spectroscopic observations, explosive evaporation is usually accompanied by blue shift with high speed (~ 100 – 400 km s $^{-1}$) in the hot lines from corona, and by red shift with low speed (~ 10 – 40 km s $^{-1}$) in the cool lines from upper chromosphere and transition region (Feldman et al. 1980; Ding et al. 1996; Del Zanna et al. 2006; Teriaca et al. 2006; Milligan & Dennis 2009; Veronig et al. 2010; Chen & Ding 2010; Brosius 2013; Doschek et al. 2013; Tian et al. 2014; Brosius & Daw 2015; Brosius et al. 2016; Zhang et al. 2016). Observationally, the speed of blue shift is an order of magnitude larger than that of red shift, which is due to the fact that the density of the overlying corona is less than that of the underlying lower chromosphere (Fisher et al. 1985a,b; Milligan & Dennis 2009; Doschek et al. 2013). Gentle evaporation occurs when the in-

put energy flux is smaller than the critical value, and all the emission lines display blue shift from chromosphere through transition region to corona (Milligan et al. 2006; Brosius 2009; Li & Ding 2011).

In the literatures, there are three mechanisms to drive chromospheric evaporation. The first one is electron-driven, which emphasizes that the nonthermal electrons accelerated by magnetic reconnection play an important role in driving chromospheric evaporation (Fisher et al. 1985b; Brosius 2003; Milligan & Dennis 2009; Tian et al. 2014, 2015; Li et al. 2015; Zhang et al. 2016). The second one focusses on the thermal energy (Fisher et al. 1985a; Falewicz et al. 2009). While the third one is driven by the energy deposition through Alfvén waves (Reep & Russell 2016). The correlation between Fe xxI 13540.9 Å Doppler velocity and HXR emission from the whole flare region has already been documented in the literatures (Li et al. 2015; Tian et al. 2015; Lee et al. 2017). In this paper, using the observations from *Interface Region Imaging Spectrograph* (*IRIS*, De Pontieu et al. 2014), *NoRH* (Hanaoka et al. 1994), *Reuven Ramaty High Energy Solar Spectroscopic Imager* (*RHESSI*, Lin et al. 2002), Atmospheric Imaging Assembly (*AIA*, Lemen et al. 2012) and Helioseismic and Magnetic Imager (*HMI*, Schou et al. 2012) aboard *Solar Dynamics Observatory* (*SDO*), we study the temporal relationship between the microwave/HXR emission and Doppler velocity of the SOL2014-10-27 event to prove the nonthermal electrons driving chromospheric evaporation around one footpoint of a solar flare loop.

2. Data Analysis and Results

The studied event takes place in NOAA AR12192 on 2014 October 27. It is an M7.1 flare in *GOES* light curve. It displays typical features of solar flares, such as two footpoint sources in microwave and HXR images. The slit of *IRIS* stays at one footpoint during the impulsive phase of the solar flare, which gives us a good chance to study the temporal evolution of the Doppler velocity in coronal and transition region lines, i.e., Fe xxI 1354.09 Å and Si iv 1402.77 Å. Figure 1 shows the *GOES* SXR fluxes in 1.0–8.0 Å (black) and 0.5–4.0 Å (turquoise), respectively. The event

starts at around 00:06 UT, and peaks at about 00:34 UT from *GOES* SXR light curves. Meanwhile, the microwave 34 GHz (purple) and HXR 25–50 keV (orange) emissions display a series of regular and periodic peaks during the impulsive phase of this solar flare, which result in several nonthermal pulses (e.g., Li et al. 2017), as marked by the Roman Capitals ‘I’, ‘II’. The first pulse (‘I’) is studied in this paper.

Figure 2 shows the multi-wavelength images from several instruments during the first pulse. They have the same field-of-view (FOV) of $90'' \times 90''$. Panel (a) displays the integral intensity image ($\sim 2.45''/\text{pixel}$) in microwave 34 GHz from 00:09 UT to 00:10 UT. The double footpoint sources are marked by the white boxes. Among them, one is bright (ft1), while the other one is faint (ft2). This is confirmed by *RHESSI* CLEAN image ($\sim 2''/\text{pixel}$) at 25–50 keV, as shown in panel (b). The contour of ft2 is from the microwave emission. Panel (c) gives the line-of-sight (LOS) magnetogram ($\sim 0.6''/\text{pixel}$) overlaid with the AIA 1600 Å contours. The bottom panels show the EUV/UV snapshots in *SDO*/AIA 131 Å and 1600 Å ($\sim 0.6''/\text{pixel}$), *IRIS*/SJI 1330 Å ($\sim 0.33''/\text{pixel}$). The AIA 1600 Å image is applied to co-align with the SJI 1330 Å image (Cheng et al. 2015; Tian et al. 2015; Li et al. 2015), because they both contain continuum emission around the temperature minimum which is dominant in many bright features. The flare ribbons in AIA 1600 Å and SJI 1330 Å are connected by the hot loops in AIA 131 Å, as indicated by the dashed lines. Consistent with the standard solar flare model, panel (e) shows that the double footpoint sources overlap on the two flare ribbons. The slit of *IRIS* crosses one flare ribbon and fixes on the edge of one footpoint (ft1), as shown by the long blue line along the 45 degree to the North-South direction.

The hot line of Fe xxI 1354.09 Å ($\log T \sim 7.05$, De Pontieu et al. 2014) in corona and the cool line of Si iv 1402.77 Å ($\log T \sim 4.8$, De Pontieu et al. 2014) in transition region are widely used to investigate chromospheric evaporation (Tian et al. 2014, 2015; Li et al. 2015; Zhang et al. 2016). Figure 3 shows the *IRIS* observation at spectral windows of ‘Fe xxI’ (a, c, e) and ‘Si iv’ (b, d, f) at three times. The Y-axis is along the slit direction. They have been pre-processed with the rou-

tines of ‘iris_orbitval_corr_l2.pro’ (Tian et al. 2014; Cheng et al. 2015) and ‘iris_prep_despike.pro’ (De Pontieu et al. 2014) in Solar Soft Ware (SSW). The absolute wavelength calibration is also manually performed with the relatively strong neutral lines, i.e., ‘O I’ 1355.5977 Å and ‘S I’ 1401.5136 Å (e.g., Tian et al. 2015). The overplotted black profile shows the spectrum at the position of about $38.6''$, which is marked by the short purple line on the left-hand side. This position is located at the edge of a flare ribbon in the northwest labeled with the short blue line in Figure 2 (e). The multi-Gaussian functions (purple profile) superimposed on a linear background (green line) are used to fit the *IRIS* spectrum at ‘Fe xxI’ window to extract the flare line of Fe xxI 1354.09 Å. The emission lines which are blended with the broad line of Fe xxI 1354.09 Å should be excluded, i.e., C I line at 1354.29 Å, Fe II lines at 1353.02 Å, 1354.01 Å, and 1354.75 Å, Si II lines at 1352.64 Å and 1353.72 Å, some unidentified lines at 1353.32 Å and 1353.39 Å (Polito et al. 2015; Young et al. 2015; Tian et al. 2015). Here, we fixed these blended line positions, constrained their widths, and tied their intensities to the lines in other spectral windows (e.g., Li et al. 2015, 2016). Finally, we can obtain the line profile of Fe xxI 1354.09 Å, as shown by the turquoise line. The transition region line of Si iv 1402.77 Å is fitted with a single-Gaussian function (purple profile) with a linear background (green line). Both the Doppler velocities of Fe xxI 1354.09 Å and Si iv 1402.77 Å are detected by the fitting line centers subtracting the referenced line centers (Li et al. 2014; Tian et al. 2015).

To exactly study the relationship between the microwave/HXR emission and the evaporation speed, Figure 4 (a) shows the normalized flux in microwave (black) and HXR (green) bands, and the temporal evolution of Doppler velocity in Fe xxI 1354.09 Å (blue) and Si iv 1402.77 Å (red) on the slit position of $38.6''$ (short purple line in Figure 3). The hot line of Fe xxI 1354.09 Å in corona displays blue shift, while the cool line of Si iv 1402.77 Å in transition region exhibits red shift, which indicates the explosive chromospheric evaporation around the footpoint of ft1. The maximum velocities of blue and red shifts are about -67 km s^{-1} and 36 km s^{-1} during the first pulse between 00:08–00:11 UT. The microwave light curves are solid (black) at ft1 and dashed

(black) at ft2. They are integrated over the regions in the white boxes in Figure 2 (a), respectively. The observations show that the pulse (between 00:08–00:11 UT) studied here completely arise from ft1, and the microwave emission at ft2 is monotonously increasing. However, the HXR flux is integrated over the whole flare region, which is the same as that in Figure 1. These light curves are well correlated during the pulse interval, but their different time cadences make the points impossible to correspond one-by-one. *NoRH*, *RHESSI* and *IRIS* have the cadences of 1 s, 4 s and 16.2 s, respectively. In this paper, we use all 9 points from the Doppler velocity around the pulse (between 00:08:30 UT and 00:11:00 UT), and their nearby points of microwave and HXR emissions. Thus, 9 points are extracted from all the light curves, as marked by the purple symbols (‘+’ or ‘×’).

Figure 4 (b) shows the Doppler velocities of Fe xxI 1354.09 Å (‘+’) and Si iv 1402.77 Å (‘×’) dependence on microwave 34 GHz (black) and HXR 25–50 keV (purple) emissions during the pulse interval, i.e., between 00:08:30 UT and 00:11:00 UT. As expected from the model of electron-driven chromospheric evaporation, we find a negative correlation (-0.96/-0.87) between the microwave/HXR emission and the Doppler velocity of hot line (Fe xxI 1354.09 Å) at ft1 (‘-’ indicates that the Doppler velocity of Fe xxI 1354.09 Å is blue shift), and a positive correlation (+0.91/+0.82) between the microwave/HXR emission and the Doppler velocity of cool line (Si iv 1402.77 Å, ‘+’ indicates that the Doppler velocity of Si iv 1402.77 Å is red shift). Such high correlation coefficients suggest that the nonthermal electrons which are accelerated by the magnetic reconnection drive the explosive chromospheric evaporation around the footpoint of ft1.

Based on the chromospheric evaporation process, the plasma upflows are expected to be observed along the flaring loops. Figure 2 (d) shows that the loops (red dashed lines) in AIA 131 Å connect the double ribbons in AIA 1600 Å. These loops become brighter and brighter with the flare development. Meanwhile, these loops expand with time. Figure 5 (a) shows the time difference image in AIA 131 Å between the pulse maximum (~00:09:32 UT) and the flare beginning (~00:06:08 UT). The two purple lines outline the

expansion loop which covers the hot plasma upflows due to chromospheric evaporation. Figure 5 (b) gives its time-distance image, and the Y-axis from bottom to top corresponds to the loop from ft2 to ft1. Thus the loop top is near the middle position in Y-axis, i.e., $\sim 41''$. It clearly shows the evaporation upflows from double footpoints through legs to loop top, as indicated by the purple arrows during 00:08:30–00:12:00 UT, which is consistent with the microwave and HXR pulse (‘I’). The evaporation speeds are estimated to be $\sim 112 \text{ km s}^{-1}$ and $\sim 99 \text{ km s}^{-1}$ without considering the projection effect.

3. Conclusions and Discussions

Based on the observations from *IRIS*, *NoRH*, and *RHESSI*, we explore the temporal relationship between Doppler velocity of Fe xxI 1354.09 Å and Si iv 1402.77 Å lines and microwave/HXR emission in microwave 34 GHz and HXR 25–50 keV during a pulse of solar flare on 2014 October 27. The completely new observational result is that the explosive chromospheric evaporation driven by nonthermal electrons originates from one footpoint of a solar flare loop. Meanwhile, the evaporation upflows are also observed from the double footpoints to loop top in AIA 131 Å image. This is consistent well with the standard solar flare model. Our results agree well with previous findings about the temporal correlation between the Doppler velocity and HXR flux which represents the deposition rate (Li et al. 2015; Tian et al. 2015; Lee et al. 2017), and are also consistent well with the studies of the spatial correlation between the upflows/dowflows and HXR sources in solar flares (Brosius & Holman 2009; Milligan & Dennis 2009; Veronig et al. 2010; Brosius et al. 2016; Zhang et al. 2016). It has been recently demonstrated that the explosive evaporation can also be driven by the dissipation through Alfvén waves, and this mechanism can produce the HXR bursts (Reep & Russell 2016). Therefore, only the presence of an HXR burst is impossible to rule out the contribution from the heating of Alfvén waves. On the other hand, a microwave pulse is observed around the peak time of *IRIS* Doppler velocity at one footpoint of a solar flare loop, implying that the nonthermal electrons are injected into the chromosphere along the flare loop in the Sun. Thus, the observations

in this case support an electron-driven chromospheric evaporation.

Figure 2 (e) and (f) shows that the slit of *IRIS* crosses one of flare ribbons. The studied position of Doppler velocity is just at the edge of flare ribbon, indicating that the explosive chromospheric evaporation appears at the outside of flare ribbon, which is consistent well with previous findings (Czaykowska 1999; Li & Ding 2004; Li et al. 2015; Tian et al. 2015). On the other hand, Figure 2 (a) exhibits that the slit of *IRIS* does not appear in the footpoint center, which may be due to the lower spatial resolution of microwave image ($\sim 4.9''$). Future work needs higher resolution observations in microwave or HXR bands, including the time and spatial resolutions.

In this letter, only the first pulse ('I') in microwave and HXR emissions is used to investigate the explosive chromospheric evaporation. We did not find any correspondence between the microwave (or HXR) emission and Doppler velocity during the other pulses, i.e., the second microwave pulse at about 00:13 UT ('II'). This may be because the upflows/downflows of the other microwave pulses are very complex. The upflows are from the new heated plasma which moves upward along the loop, while the downflows from the last evaporated material may eventually cool and precipitate back down along the loop (e.g., Brosius 2003; Milligan & Dennis 2009). It could also be because the location of energy deposition is not covered by the slit of *IRIS*. The good correlation between Doppler velocity and microwave/HXR emission may be found when shifting the slit position (e.g., Li et al. 2015).

The authors would appreciate the anonymous referee for his/her valuable comments and suggestions to improve the manuscript. We thank the teams of *IRIS*, *GOES*, *NoRH*, *RHESSI*, *SDO/AIA* and its *SDO/HMI* for their open data use policy. The authors also thank Y. Gong for reading our manuscript. This study is supported by NSFC under grants 11603077, 11573072, 11473071, 11333009, KLSA201708, and Laboratory No. 2010DP173032. Dr. D. Li is also supported by the Youth Fund of Jiangsu No. BK20161095, and Dr. Q. M. Zhang is supported by the Surface Project of Jiangsu No. BK 20161618 and the Youth Innovation Promotion Association CAS.

REFERENCES

- Antonucci, E., Gabriel, A. H., Acton, L. W., et al. 1982, *Sol. Phys.*, 78, 107
- Aschwanden, M. J., & Benz, A. O. 1995, *ApJ*, 438, 997
- Asai, A., Nakajima, H., Shimojo, M., et al. 2006, *PASJ*, 58, L1
- Brosius, J. W. 2003, *ApJ*, 586, 1417
- Brosius, J. W. 2009, *ApJ*, 701, 1209
- Brosius, J. W., & Holman, G. D. 2009, *ApJ*, 692, 492
- Brosius, J. W. 2013, *ApJ*, 762, 133
- Brosius, J. W., & Daw, A. N. 2015, *ApJ*, 810, 45
- Brosius, J. W., Daw, A. N., & Inglis, A. R. 2016, *ApJ*, 830, 101
- Brown, J. C. 1971, *Sol. Phys.*, 18, 489
- Brown, J. C. 1973, *Sol. Phys.*, 31, 143
- Chen, F., & Ding, M. D. 2010, *ApJ*, 724, 640
- Cheng, X., Ding, M. D., & Fang, C. 2015, *ApJ*, 804, 82
- Czaykowska, A., & De Pontieu, B., & Alexander, D., & Rank, G. 1999, *ApJ*, 521, L75
- De Pontieu, B., & Title, A. M., & Lemen, J. R., et al. 2014, *Sol. Phys.*, 289, 2733
- Del Zanna, G., & Schmieder, B., & Mason, H., & Berlicki, A., & Bradshaw, S. 2006, *Sol. Phys.*, 234, 95
- Ding, M. D., & Watanabe, T., & Shibata, K., et al. 1996, *ApJ*, 458, 391
- Doschek, G. A., & Warren, H. P., & Young, P. R. 2013, *ApJ*, 767, 55
- Falewicz, R., & Rudawy, P., & Siarkowski, M. 2009, *A&A*, 508, 971
- Feldman, U., & Doschek, G. A., & Kreplin, R. W., & Mariska, J. T. 1980, *ApJ*, 241, 1175
- Fisher, G. H., & Canfield, R. C., & McClymont, A. N. 1985a, *ApJ*, 289, 414

- Fisher, G. H., & Canfield, R. C., & McClymont, A. N. 1985b, *ApJ*, 289, 425
- Hanaoka, Y., Shibasaki, K., Nishio, M., et al. 1994, *Proceedings of Kofu Symposium*, 35
- Karlicky, M. 1998, *A&A*, 338, 1084
- Lee, K.-S., Imada, S., Watanabe, K., Bamba, Y., & Brooks, D. H. 2017, *ApJ*, 836, 150
- Lemen, J. R., & Title, A. M., & Akin, D. J., et al. 2012, *Sol. Phys.*, 275, 17
- Li, Y., & Ding, M. D. 2011, *ApJ*, 727, 98
- Li, L. P., Peter, H., Chen, F., & Zhang, J. 2014, *A&A*, 570, A93
- Li, D., Ning, Z. J., & Zhang, Q. M. 2015, *ApJ*, 813, 59
- Li, D., Innes, D. E., & Ning, Z. J. 2016, *A&A*, 587, A11
- Li, D., Zhang, Q. M., Huang, Y., Ning, Z. J., & Su, Y. N. 2017, *A&A*, 597, L4
- Li, J. P., & Ding, M. D. 2004, *ApJ*, 606, 583
- Lin, R. P., & Dennis, B. R., & Hurford, G. J., et al. 2002, *Sol. Phys.*, 210, 3
- Liu, W., & Liu, S. M., & Jiang, Y. W., et al. 2006, *ApJ*, 649, 1124
- Milligan, R. O., & Gallagher, P. T., & Mathioudakis, M., et al. 2006, *ApJ*, 642, L169
- Milligan, R. O., & Dennis, B. R. 2009, *ApJ*, 699, 968
- Milligan, R. O. 2015, *Sol. Phys.*, 290, 3399
- Ning, Z. J., & Cao, W. D., & Huang, J., et al. 2009, *ApJ*, 699, 15
- Ning, Z. J., & Cao, W. D. 2010, *ApJ*, 717, 1232
- Ning, Z. J. 2011 *Sol. Phys.*, 273, 81
- Nitta, S., Imada, S., & Yamamoto, T. T. 2012, *Sol. Phys.*, 276, 183
- Polito, V., Reeves, K. K., Del Zanna, G., Golub, L., & Mason, H. E. 2015, *ApJ*, 803, 84
- Schou, J., Scherrer, P. H., Bush, R. I., et al. 2012, *Sol. Phys.*, 275, 229
- Reep, J. W., & Russell, A. J. B. 2016, *ApJ*, 818, L20
- Teriaca, L., & Falchi, A., & Falciani, R., & Cauzzi, G., & Maltagliati, L. 2006, *A&A*, 455, 1123
- Tian, H., & Li, G., & Reeves, K. E., et al. 2014, *ApJ*, 797, L14
- Tian, H., Young, P. R., Reeves, K. K., et al. 2015, *ApJ*, 811, 139
- Veronig, A. M., & Rybák, J., & Gömöry, P., et al. 2010, *ApJ*, 719, 655
- Young, P. R., Tian, H., & Jaeggli, S. 2015, *ApJ*, 799, 218
- Zhang, Q. M., Li, D., Ning, Z. J., et al. 2016, *ApJ*, 827, 27

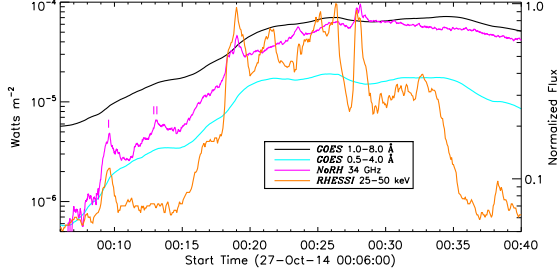


Fig. 1.— SXR light curves of 2014 October 27 flare from 00:06 UT to 00:40 UT in 1.0–8.0 Å (black) and 0.5–4.0 Å (turquoise). Normalized flux in microwave of 34 GHz (purple) and HXR 25–50 keV (orange) from the whole flare region during the same time intervals.

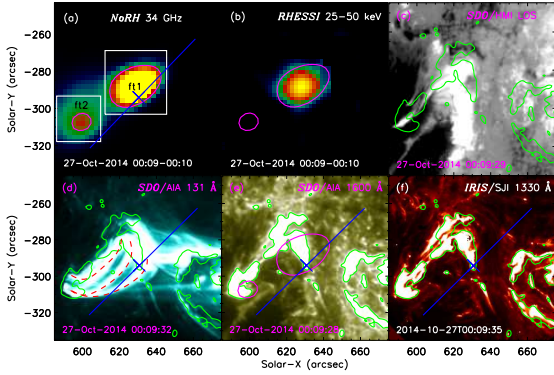


Fig. 2.— The multi-wavelength images with a FOV of $90'' \times 90''$ on the 2014 October 27 flare. The purple contours are from the microwave of 34 GHz, and the white boxes indicate the sources of two footpoints. The green contours represent the AIA 1600 Å intensities at the scale of 200 DN s^{-1} . The red dashed lines in AIA 131 Å outline the possible flare loops. The long blue line represents the slit of *IRIS* and the short blue line marks the region studied here.

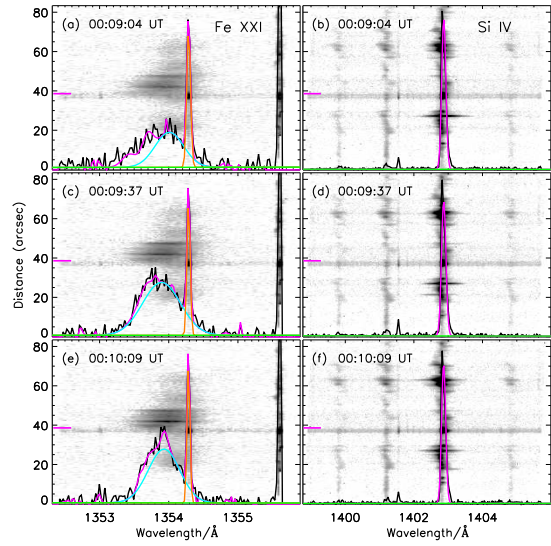


Fig. 3.— *IRIS* spectra at ‘Fe XXI’ (left) and ‘Si IV’ (right) windows on 2014 October 27. The black profile is the line spectrum across the slit position marked by a purple line on the left-hand side of each image, the overplotted purple profile represents the fitting results. The turquoise line is Fe XXI 1354.09 Å, and the orange line is C I 1354.29 Å. The green line is the fitting background.

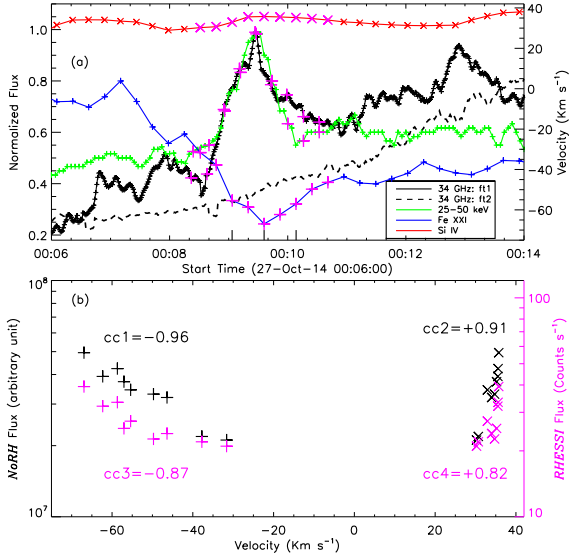


Fig. 4.— Panel (a): The microwave emission in *NoRP* 34 GHz at ft1 (solid black) and ft2 (dashed black) during 00:06–00:14 UT. The HXR flux in *RHESSI* 25–50 keV (green) is from the whole flare at the same time. The temporal evolution of Doppler velocities at Fe XXI 1354.09 Å (blue) and Si IV 1402.77 Å (red) lines are detected from a distinct position along the slit of *IRIS*. Panel (b): Scatter plots of Doppler velocities dependence on microwave and HXR emissions during the first pulse. The correlation coefficients (cc) are labeled.

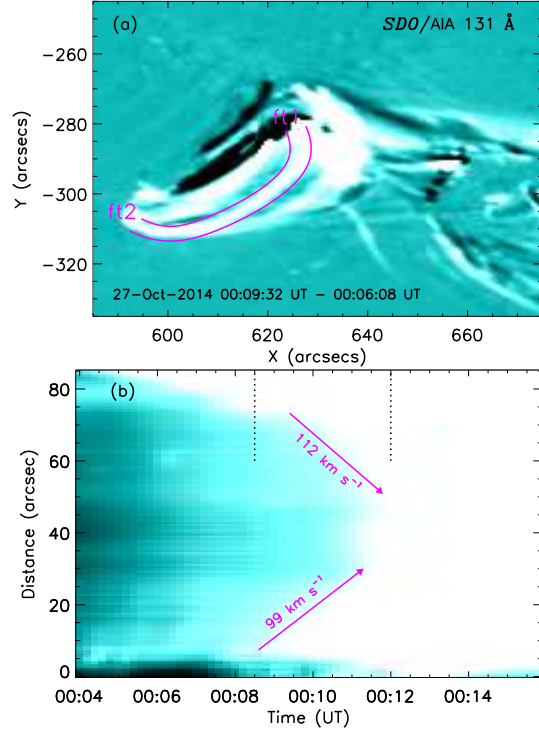


Fig. 5.— Upper: The difference map in AIA 131 Å, two solid lines (purple) outline a flare loop. Bottom: The time-distance image along flare loop in AIA 131 Å. The start point ($d=0$) is from ft2. The arrows indicate the upflow directions. Two dotted lines mark the upflow time between 00:08:30–00:12:00 UT.